Microporous and Mesoporous Materials 331 (2022) 111669

Contents lists available at ScienceDirect

Microporous and Mesoporous Materials

journal homepage: www.elsevier.com/locate/micromeso

A pyridinyl-phenanzine conjugated microporous polymer decorated with ultrafine Ag nanoparticles mediates the rapid reduction of nitrophenol

Mohammed G. Kotp [a], Ahmed F.M. EL-Mahdy [a,**], Tzu-Ling Yang [a], Shiao-Wei Kuo [a,b,*]

[a] Department of Materials and Optoelectronic Science, Center for Functional Polymer and Supramolecular Materials, National Sun Yat-Sen University, Kaohsiung, 80424, Taiwan

[b] Department of Medicinal and Applied Chemistry, Kaohsiung Medical University, Kaohsiung, 807, Taiwan

ARTICLE INFO

Keywords:
Conjugated microporous polymers
Silver nanoparticle
Nanocatalysts
p-nitrophenol

ABSTRACT

In this study we used classical Suzuki polycondensation to prepare a pyridinyl-phenanzine (TPPQP) conjugated microporous polymer (CMP) that featured a spherical morphology with a large surface area (371 $m^2\ g^{-1}$) and high thermal stability (T_{d10} = 625 °C; char yield = 81.7 wt%). The framework of the TPPQP CMP presented many dynamic pyridinic units could capture Ag^+ ions from solution and facilitate their self-reduction to Ag nanoparticles, thereby forming Ag@TPPQP CMP nanocatalysts. The Ag@TPPQP CMP nanocatalysts were strong reducing agents for pollutant nitrophenols, converting them into safe amino forms at standard temperature and pressure with a high normalized rate of 19.4 $mg^{-1}\ s^{-1}$. The pyridinic units in the TPPQP CMP structure played an important role in the catalytic reaction, interacting with the phenolic OH groups of *p*-nitrophenol to accelerate the reduction.

1. Introduction

Nitroaromatic materials are hydrocarbon pollutants of high toxicity and carcinogenicity, leading to greater calls for their disposal [1–6]. The accumulation of *para*-nitrophenol (*p*-NP) through the food chain and its prevalence in the nervous system can result in liver and kidney failure and other mortal diseases [7,8]. Although the dye and herbicide industries produce massive quantities of *p*-NP, the Environmental Protection Agency (EPA) has graded *p*-NP as a highly hazardous contaminant and has limited its ultimate concentration to 10 parts per billion in potable water [9–11]. Bacterial remediation [12], microwave-assisted catalytic oxidation [13], electrochemical oxidation [14], gamma irradiation [15], catalytic ozonation [16], photocatalytic oxidation [17], and reduction have all been suggested for the disposal of *p*-NP, but some of these processes have considerable defects. For example, bacterial remediation is limited at low concentrations of *p*-NP (<200 mg L^{-1}), with every kind of nitroaromatic compound requiring a different kind of bacteria. The high operational costs of microwave-assisted catalytic oxidation and electrochemical oxidation process limit their engineering applications. The applications of electricity and gamma irradiation can be unsafe. Although heterogeneous catalytic ozonation can effectively degrade nitroaromatic compounds, this process can display instability and unsustainability during consecutive runs. Finally, the photocatalytic oxidation of *p*-NP is limited at very low concentrations (<20 mg L^{-1}).

Practically, processes for the reduction of *p*-NP have been most applicable because of their low energy requirements, economy, effectiveness, safety, and ease of operation [6,18,19]. Nevertheless, industries that use *p*-NP are still requiring procedures with higher reduction rates [5]. Realistically, the reduction of *p*-NP will remain a pivotal reaction for disposing of this toxic compound; furthermore, the product of this reaction, *para*-aminophenol (*p*-AP), is a highly useful industrial molecule [20,21] for various applications, including dyes [22], drugs [23], photography [24], and anti-corrosion materials [25], and as an optoelectronic material for polybenzoxazine, phenolic resin, and poly(cyanate ester) [26–29]. Although the reduction of *p*-NP is economical, a small amount of energy (to obtain the requisite temperature or H_2 pressure) must be consumed to accelerate the rate of reduction. Alternatively, the rate of reduction might be accelerated by lowering the kinetic barrier of the reducing agent toward its electron acceptor. Indeed, various noble metals (Pd, Pt, Ru, Au, Ag) are useful catalysts for these kinds of reduction reactions, albeit generally

* Corresponding author. Department of Materials and Optoelectronic Science, Center for Functional Polymer and Supramolecular Materials, National Sun Yat-Sen University, Kaohsiung, 80424, Taiwan.
** Corresponding author.
E-mail addresses: ahmedelmahdy@mail.nsysu.edu.tw (A.F.M. EL-Mahdy), kuosw@faculty.nsysu.edu.tw (S.-W. Kuo).

https://doi.org/10.1016/j.micromeso.2021.111669
Received 22 November 2021; Received in revised form 23 December 2021; Accepted 28 December 2021
Available online 4 January 2022

expensive [18,30,31]. For this present study we wished to choose a lower-cost metal that operates through a simple reduction pathway from its corresponding ion solution, ultimately settling on Ag [32,33], which is relatively abundant, inexpensive, electrically active, and thermally stable when compared with other noble metals [32,34,35]. Because Ag nanoparticles (NPs) tend to agglomerate readily, they are often anchored onto various carriers, including carbonaceous materials, silica substrates, magnetite, and covalent organic frameworks (COFs) to restrict their assembly [36,37]; therefore, we wished to develop a suitable surface for their attachment.

In the last decade, porous organic polymers featuring a broad range of networks, including COFs, covalent triazine frameworks, hypercrosslinked polymers, porous aromatic frameworks, and conjugated microporous polymers (CMPs), have garnered attention for their use in various technologies [38–49]. Cao et al. [36] reported that CMPs stabilized the uptake of ultrafine Ag NPs and prevented them from agglomeration. Indeed, CMPs have been prominent among the porous materials because of their π-conjugated frameworks and microporous structures [42,50–52]. Moreover, the extensive range of potential building subunits of CMP frameworks has led to their high applicability in such fields as gas adsorption [53], photo redox catalysis [54,55], energy storage [56–58], biology [59], energy production [50,60,61], and heterogeneous catalysis [62,63]. For example, Cao et al. [36] decorated a cyano-pyridyl CMP with Ag NPs, but observed only a low rate of catalytic reduction of *p*-NP (1.84 mmol s^{-1}). Furthermore, Gong et al. [64] prepared a CMP featuring carbazole (CZ) and 1,3,5-triethynylbenzene (TEB) units (CZ-TEB CMP), decorated it with Ag NPs, and then employed the decorated Ag@CZ-TEB CMP for the reduction of *p*-NP; here, they used harmful $NaBH_4$ as the reducing agent to deposit the Ag NPs onto the CZ-TEB CMP. To improve the rate of reduction of *p*-NP, in this study we sought a more suitable CMP for decoration with Ag NPs without using harmful reducing agents. Accordingly, we designed a new CMP featuring a large number of pyridyl units. Liu et al. [65,66] had previously synthesized planar polymers based on 3,6,14,17-tetrabromodibenzo[*a*,*c*]-dibenzo[5,6:7,8]quinoxalino-[2,3-*i*]- phenazine (3-TBQP) for energy storage applications. We suspected that the 3-TBQP monomer, which offers many pyridinic units per molecule, might display high performance toward capturing Ag^+ ions.

Here, we designed a new two-dimensional CMP (TPPQP) using the boron ester 2,4,6-tris(4-(4,4,5,5-tetramethyl-1,3,2-dioxaborolan-2-yl) phenyl)pyridine (TPP-3Bpin) and 3-TBQP. We fabricated the TPPQP CMP through Suzuki polycondensation of these monomers under solvothermal conditions. The TPPQP CMP possessed a high surface area; furthermore, decoration of TPPQP CMP with Ag NPs was possible through a simple, inexpensive, and eco-friendly one-step reaction—in contrast to many other approaches that have depended on using harmful traditional reducing agents (e.g., hydrazine and $NaBH_4$) [64,67,68] or microwave assistance [69] for producing Ag NPs. Inductively coupled plasma (ICP) spectroscopy revealed the weight percentages of the decorated Ag NPs on the TPPQP CMP after soaking in solutions containing various concentrations of silver nitrate ($AgNO_3$). The alkaline pyridyl groups present in the Ag@TPPQP CMP nanocatalyst enhanced the kinetics of the reduction of *p*-NP through interactions with the phenolic OH group.

2. Experimental

2.1. TPP-3Br

Using a previously published procedure [39], a mixture of 4-bromoacetophenone (4.14 g, 20.8 mmol), ammonium acetate (28.0 g, 363 mmol), and acetic acid (14.6 mL, 0.260 mmol) was continuously stirred and then placed in a 20-mL microwave flask. Under self-generated pressure at 500 W, the reaction mixture was heated at 220 °C for 45 min. The container was cooled to ambient temperature under a flow of water and then small amounts of $NaHCO_3$ were added until the suspension had been neutralized. The precipitate was extracted into CH_2Cl_2. The solvent was evaporated, and the product recrystallized from acetone (Scheme S1). FTIR (powder): 1644, 1596, 1483, 813 cm^{-1} (Fig. S1). ^1H NMR ($CDCl_3$, 25 °C, 600 MHz, ppm): δ 8.037 (d, 4H), 7.8 (s, 2H), 7.647 (d, 2H), 7.65 (d, 4H), 7.58 (d, 2H). ^{13}C NMR ($CDCl_3$, 25 °C, 500 MHz, ppm): δ 156.5, 149.5, 137.84, 137.28, 132.28, 131.82, 128.5, 123.9, 123.5, 116.73.

2.2. TPP-3Bpin

As displayed in Scheme S2, TPP-3Br was subjected to boronation to obtain TPP-3Bpin. TPP-3Br (1.20 g, 2.20 mmol) and bis(pinacolato) diboron (2.57 g, 10.1 mmol) were placed in a two-neck flask. [1,1′-Bis (diphenylphosphino)ferrocene]dichloropalladium(II) (0.142 g, 0.193 mmol) and potassium acetate (0.900 g, 9.15 mmol) were added and then the flask was subjected to degassing for 15 min. Under continuous magnetic stirring, dioxane (50 mL) was injected into flask, which was then left at 110 °C for 2 days. The solid was filtered off, and washed several times with water and MeOH, and then purified chromatographically (SiO_2; THF/hexane, 1:3). Vacuum rotary evaporation of the eluent gave a white precipitate, which was dispersed in MeOH for 24 h. The product was filtered off and dried at 50 °C for 10 h. FTIR (powder): 2977, 1600, 1614, 1399, 1212, 1141 cm^{-1} (Fig. S1). ^1H NMR (CD_3Cl, 25 °C, 400 MHz, ppm): δ 8.2 (d, 4H), 7.9 (d, 2H), 7.93 (s, 2H), 7.75 (d, 4H), 1.37 (s, 12H) (Fig. S3). ^{13}C NMR ($CDCl_3$, 25 °C, 500 MHz, ppm): δ 158.4, 150.6, 142.2, 136.1, 127.7, 118.4, 84.79, 24.69 (Fig. S4).

2.3. 3-TBQP

3-TBQP was synthesized (Scheme S3) according to a previously reported procedure [65]. 3,6-Diibromophenanthrene-9,10-dione (3,6-DBPD; 0.760 g, 2.10 mmol) and benzene-1,2,4,5-tetraamine tetrahydrochloride (0.280 g, 1.00 mmol) were mixed in a 100-mL round-bottom two-neck flask under magnetic stirring. EtOH (6 mL) and acetic acid (20 mL) were added and then the mixture was heated at 100 °C. The flask was kept under a N_2 atmosphere, followed by the injection of triethylamine (1.0 mL), resulting in a red color appearing immediately. The mixture was heated under reflux at 130 °C for 6 h. The product was filtrated and dried at 80 °C for 12 h. FTIR (powder): 1698, 1578, 1488, 820 cm^{-1} (Fig. S2).

2.4. TPPQP CMP

The TPPQP CMP was prepared as presented in Scheme 1. TPP-Bpin (200 mg, 4.00 mmol) was added to 3-TBQP (174.7 mg, 3 mmol) and tetrakis(triphenylphosphine)palladium [$Pd(PPh_3)_4$; 50 mg, 0.30 mmol] in a Schlenk tube. Potassium carbonate (303 mg, 30.0 mmol) was added and then the contents were degassed for 15 min. The co-solvents DMF (10 mL) and water (1.25 mL) were injected into the tube. The mixture was subjected to three freeze/pump/thaw cycles and then heated at 140 °C for 72 h under a N_2 atmosphere with continuous magnetic stirring. The reddish-brown precipitate was filtered off, washed several times with water, washed again in a Soxhlet system using MeOH and hexane, then dried at 80 °C for 24 h. FTIR (powder): 1730, 1632 cm^{-1} (Fig. 1a).

2.5. Ag@TPPQP CMP nanocatalyst

A series of $AgNO_3$ solutions was prepared with concentrations of 0.1, 0.3, and 0.5 mmol L^{-1}. The TPPQP CMP (10 mg) was soaked in the individual solutions of $AgNO_3$ (10 mL). The mixtures were stirred magnetically for 24 h. The three composites were separated through centrifugation, washed with water, and then dried at 50 °C, yielding the samples *x*Ag@TPPQP CMP ($x = 1, 3, 5$). ICP spectroscopy revealed that Ag contents in the 1Ag@TPPQP, 3Ag@TPPQP, and 5Ag@TPPQP CMPs were 0.232, 0.336, and 0.482 wt%, respectively. FTIR (powder): 1735,

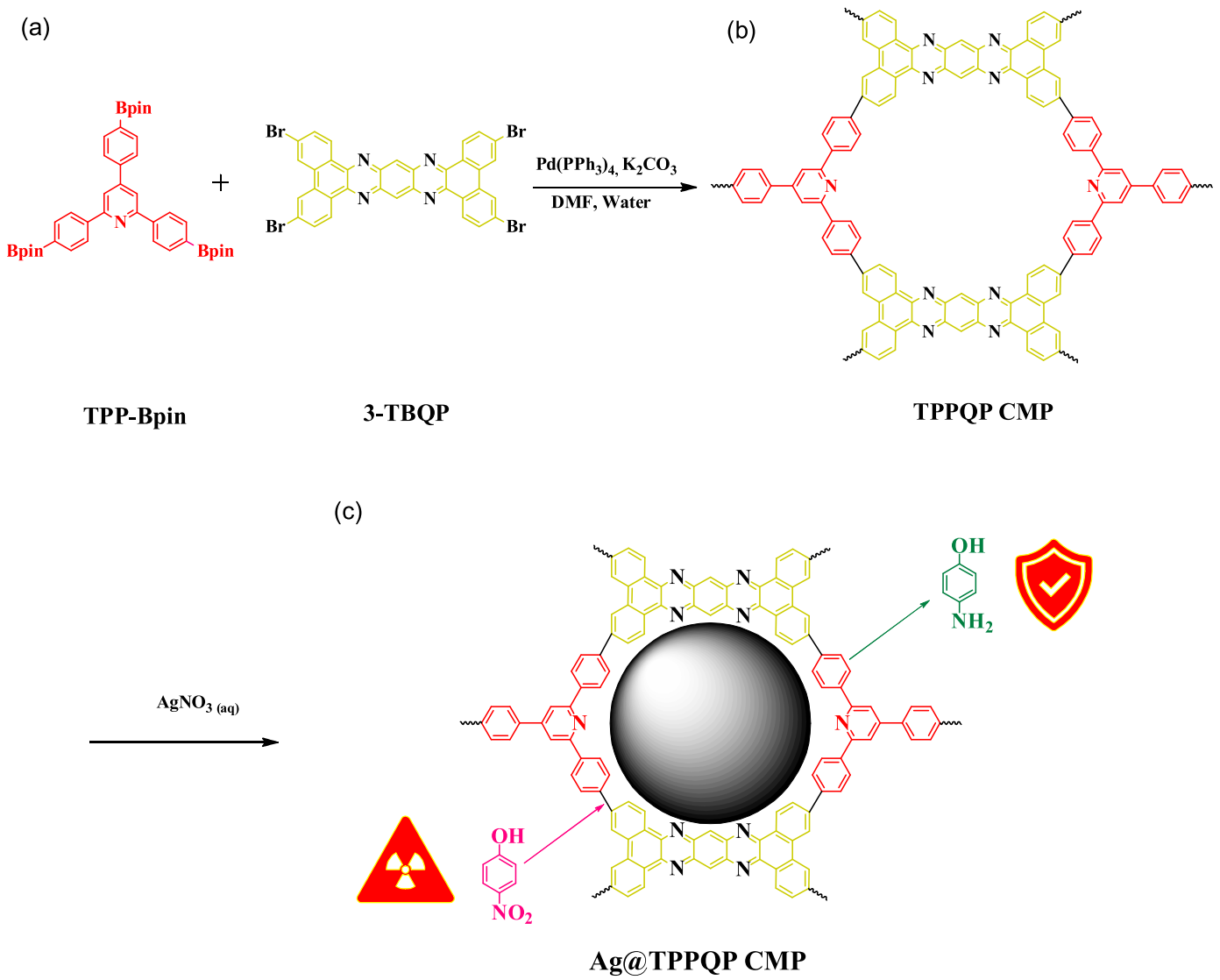

Scheme 1. Synthesis and chemical structures of (a) TPP-Bpin and 3-TBQP, (b) the TPPQP CMP, and (c) the Ag@TPPQP CMP.

1638 cm^{-1} (Fig. 1a).

2.6. Ag@TPPQP CMP–mediated reduction of p-NP to p-AP

p-NP (2.0 mL, 0.16 mM) and $NaBH_4$ (0.5 mL, 0.08 M) were mixed in a quartz macro-cuvette, then an *x*Ag@TPPQP CMP nanocatalyst (0.5 mL, 1 mg/mL) was added. The same concentration of *p*-NP was used for the three samples of Ag NPs loaded onto the TPPQP CMPs. The progress of the reactions was followed using a UV–Vis spectrophotometer.

2.7. Recovery of Ag@TPPQP nanocatalyst

To determine the recovery, the quantities of the materials were increased sevenfold. The 1Ag@TPPQP CMP nanocatalyst was subjected to five runs; it was separated (centrifugation) and washed (water and EtOH) after each cycle to avoid nanocatalyst loss, then dried prior to the next cycle.

3. Results and discussion

We prepared the TPPQP CMP through palladium-catalyzed Suzuki polycondensation of TPP-3Bpin with 3-TBQP (Scheme 1). We expected that the pyridyl units of the TPPQP CMP, present in both of its subunits, would behave as active sites for the capture of Ag^+ ions and their subsequent reduction to Ag NPs. Furthermore, we expected that the pyridyl units would also improve the rate of reduction of *p*-NP through interactions with the phenolic OH units. We used three different concentrations of $AgNO_3$ (0.1, 0.3, and 0.5 mM) to prepare the nanocatalysts denoted *x*AgTPPQP CMP ($x = 1, 3, 5$).

3.1. Characterization of TPP-3Bpin and 3-TBQP monomers

TPP-3Bpin was synthesized from previously reported TPP-3Br, as presented in Schemes S1 and S2. We characterized TPP-3Br and TPP-3Bpin using FTIR spectroscopy; both monomers provided vibrational signals for C–H, C═N, and C═C bonds at 2977, 1600, and 1399 cm^{-1}, respectively (Fig. S1). Furthermore, the spectrum of TPP-3Bpin featured signals for stretching vibrations of C–H aromatic, C–N, B–O, C–B, and C–O bonds at 2977, 1600, 1399, 1212, and 1141 cm^{-1}, respectively Fig. S2 displays the ^1H NMR spectrum of TPP-3Bpin; signals for protons of the methyl groups, pyridyl ring, and substituents on the aromatic ring appear at 1.37, 7.69, and 8.20–7.75 ppm, respectively. The corresponding ^{13}C NMR spectrum of TPP-3Bpin (Fig. S3) features signals for the carbon nuclei in the methyl groups, boron ring, C═N unit, and aryl rings at 24.7, 84.5, and 158.4, respectively, with other peaks appearing at 151.0, 142.4, 127.1, and 118.2 ppm. These spectral data confirmed

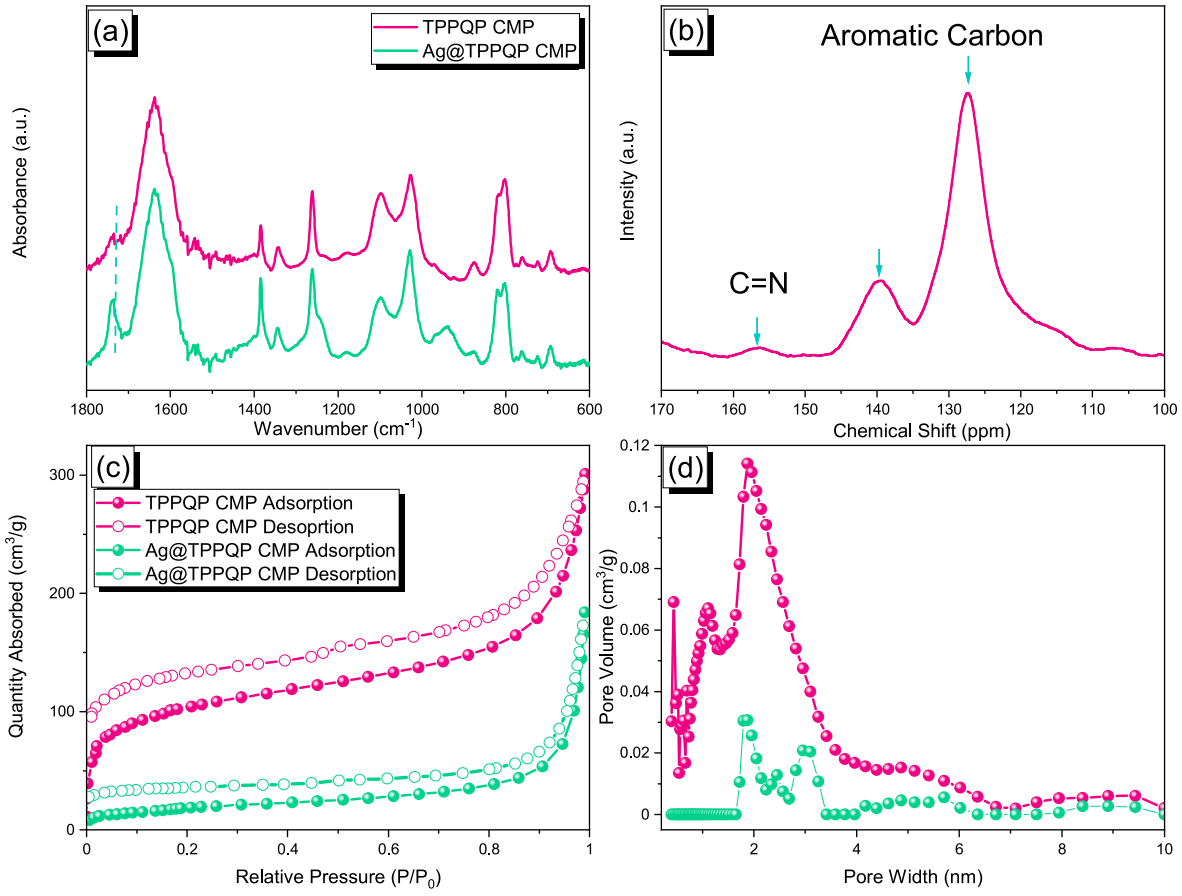

Fig. 1. (a) FTIR spectra of the TPPQP CMP before and after decoration with Ag NPs. (b) Solid state ^{13}C NMR spectrum of the TPPQP CMP. (c) N_2 sorption isotherms recorded at 77 K. (d) Pore size distributions of the TPPQP CMP before and after anchoring Ag NPs.

the synthesis of TPP-3Bin. Scheme S3 displays the synthesis of the monomer 3-TBQP. Because the solubility of 3-TBQP in water and common solvents was poor, we used FTIR spectroscopy alone to characterize its chemical structure (Fig. S4). The spectrum featured signals for the stretching vibrations of C═N, C═C, and aryl units at 1698, 1578, and 820 cm^{-1}, respectively, consistent with complete condensation and formation of 3-TBQP.

3.2. Characterization of the TPPQP CMP

We used FTIR spectroscopy to characterize the as-synthesized TPPQP CMP (Fig. 1a). The disappearance of the signals for the B–O, C–B, and C–O vibrations of TPP-Bpin indicated its complete consumption in the Suzuki reaction; signals for the stretching vibrations of the C═N and C═C bonds of the aryl rings at 1730 and 1632 cm^{-1}, respectively, were primary indicators of the formation of the TPPQP CMP (Fig. 1b). displays the solid state ^{13}C NMR spectrum of the TPPQP CMP, with the signal at 156 ppm representing C═N units and the other broad signals at 139.6–127.4 ppm representing acyl carbon nuclei. Field emission scanning electron microscopy (FE-SEM) revealed the spherical morphology of the TPPQP CMP (Fig. 2a). The interparticle structure of the TPPQP CMP was revealed using transmission electron microscopy (TEM) (Fig. 2c)], suggesting good dispersity of TPPQP CMP without considerable agglomeration. The thermal stability of the TPPQP CMP was high, as indicated by a decomposition temperature (T_{d10}) of 625 °C; in addition, a char yield of 81.7 wt% was determined after heating to 800 °C (Fig. S5). The high thermal stability of the TPPQP CMP suggested a high degree of condensation and high planarity. The microporosity of the TPPQP CMP was estimated through N_2 adsorption at 77 K; according to IUPAC classification, it underwent type-I N_2 gas sorption (Fig. 1c). We used the Brunauer–Emmett–Teller (BET) method to measure the surface area (371 $m^2\ g^{-1}$) and pore volume (0.5124 $cm^3\ g^{-1}$) of the TPPQP CMP. Furthermore, the pore size distribution of the TPPQP CMP, based on nonlocal density functional theory, featured multiple peaks near 1.13, 1.84, and 4.87 nm (Fig. 1d, suggesting the presence of the microporous/mesoporous structures.

3.3. Characterization of Ag@TPPQP CMP nanocatalysts

We employed a green decoration method, without any harmful reducing agents, to obtain the *x*Ag@TPPQP CMP nanocatalysts. The Ag^+ ions were captured by pyridyl groups spread throughout the TPPQP CMP; upon irradiation with visible light, these units facilitated the reduction of the Ag^+ ions to give Ag NPs. Fig. 1a displays the FTIR spectra of the Ag@TPPQP CMPs; only slight shifts in the positions of the signals (from 1730 to 1735 cm^{-1}) occurred relative to that of the pristine TPPQP CMP. As expected, the BET surface area of the 1Ag@TPPQP CMP decreased to 67 $m^2\ g^{-1}$(Fig. 1c); the pore size distribution increased to 1.83, 3.02, and 5.28 nm after decoration of the Ag NPs on the surface of the TPPQP CMP. Fig. 2b reveals the spherical morphology of the Ag@TPPQP CMP, based on FE-SEM imaging. Fig. 2(d)–(f) present corresponding TEM images, revealing good dispersity of the Ag NPs at various percentages on the surface of the TPPQP CMPs, without considerable aggregation, due to the high surface area and porosity of the TPPQP CMP. The Ag NPs at various concentrations on the TPPQP CMP were also examined using high-resolution TEM (HR-TEM) [Fig. 2 (g)–(i)]; the interplanar distance between the strips, calculated from the lattice fringes of *x*Ag@TPPQP CMP, was 0.24 nm, consistent with the lattice plane [111] of cubic Ag [70]. Furthermore, the TEM images provided statistical data for calculating the sizes of the Ag NPs, with

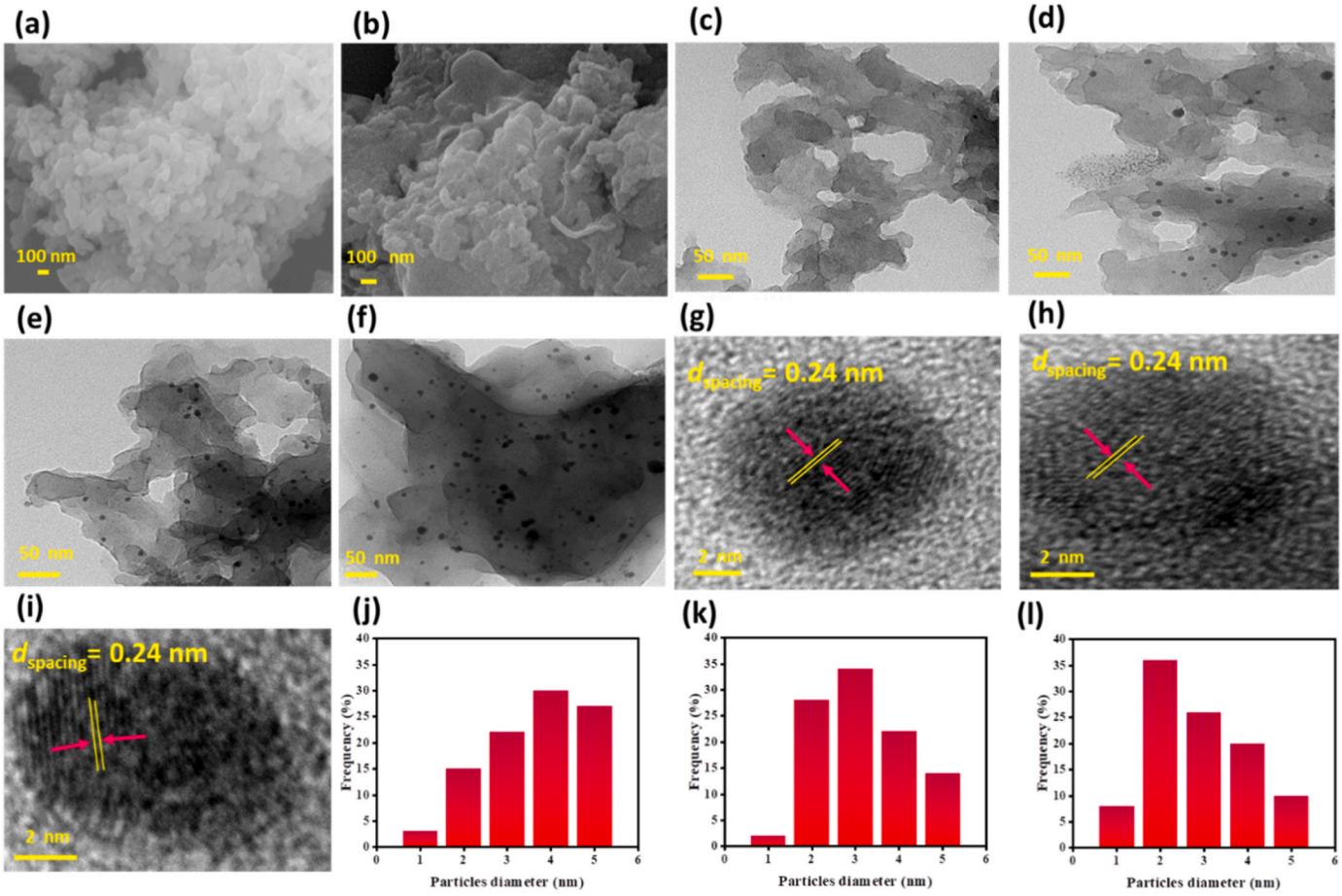

Fig. 2. (a, b) FE-SEM images of the TPPQP CMP (a) before and (b) after decoration with 1 wt% Ag NPs. (c–f) TEM and (g–i) HR-TEM images and (j–l) diameter distributions of (c) the pure TPPQP CMP and (d, g, j) the 1 wt% of Ag@TPPQP CMP, (e, h, k) the 3 wt% of Ag@TPPQP CMP, and (f, i, l) the 5 wt% of Ag@TPPQP CMP nanocatalysts.

average dimensions of approximately 2–3 nm for the 1Ag@TPPQP, 3Ag@TPPQP, and 5Ag@TPPQP CMPs nanocatalysts [Fig. 2(j)–(l), respectively; 100 particles used to obtain the statistical data]. Furthermore, TEM visualization of bare TPPQP CMP (Fig. 2c) does not display any Pd nanoparticles confirming the negligible percentages of Pd residue confirming the negligible influence of it within reduction process. These percentages of Ag loaded in 1Ag@TPPQP, 3Ag@TPPQP, and 5Ag@TPPQP, calculated using ICP spectroscopy, were 0.232, 0.336, and 0.482 wt% respectively; thus, a greater concentration of the $AgNO_3$ solution led to the production of more Ag NPs on the TPPQP CMP. The contents of C, N, and Ag atoms in the 1Ag@TPPQP CMP, measured using SEM-EDX, were 53.19, 46.34, and 0.47 wt%, respectively (Fig. S6, Table S1); this content of Ag matches that determined using ICP spectroscopy. Elemental mapping of the 1Ag@TPPQP CMP nanocatalyst revealed the dispersions of the C, N, and Ag atoms (Fig. S6).

We used XPS to elucidate the surface components of the Ag@TPPQP CMP nanocatalysts. Fig. 3 displays the high-resolution XPS profiles for every element in our nanocatalysts. Two peaks appeared at 284.4 and 285.8 eV [Fig. 3(a)–(c)] for the C–C═C and N–C═N units, respectively, in the 1Ag@TPPPQP, 3Ag@TPPQP, and 5AgTPPQP CMP nanocatalysts. Fig. 3(d)–(f) all feature a characteristic peak near 399.5 eV for the pyridinic nitrogen atoms in this series of nanocatalysts. The Ag atoms in the 1Ag@TPPQP, 3Ag@TPPQP, and 5Ag@TPPQP CMP nanocatalysts featured two characteristic binding energies of 368 eV ($3d_{5/2}$) and 374 eV ($3d_{3/2}$), as revealed in Fig. 3(g)–(i), respectively. Table S2 summarizes the results obtained from curve fitting of the signals of all of the elements in Fig. 3; we conclude that the different amounts of Ag NPs did not strongly affect the binding energies of any of the elements.

3.4. Catalytic performance in the reduction of p-NP

As mentioned above, nitrophenols are very important in many fields, but disposing of them in common degradation systems is not always easy because of their biological and chemical resistance; thus, reduction of nitrophenols to a safe form is necessary in our quest for sustainable chemistry [71]. Accordingly, we selected the reduction of *p*-NP as a model to examine the catalytic performance of our Ag@TPPQP CMP nanocatalysts. The Langmuir–Hinshelwood mechanism explains well the catalytic reaction of the reduction of *p*-NP in the presence of the Ag@TPPQP CMP nanocatalysts (Equations S1–S5). Briefly, the Ag NPs absorbed BH_4^- ions; these ions adsorbed onto the surface of the nanocatalysts formed activated H_2, which underwent the hydrogenation of *p*-NP [72]. UV–Vis spectral profiles revealed the progress of the reduction of *p*-NP in the presence of $NaBH_4$ and the Ag@TPPQP CMP nanocatalysts. The transformation of the UV spectral signal from 316 to 400 nm (Fig. 4a) upon addition of $NaBH_4$ represents the conversion of *p*-NP to *p*-nitrophenolate. The catalytic performance of our TPPQP CMP (Fig. S8) was used as control comparing with Ag@TPPQP CMP nanocatalyst, As displayed in Fig. S8, the characteristic band of p-NP at 400 nm has not any noticeable decrease within reaction time, consequently the catalytic efficacy were attributed so Ag@TPPQP CMP nanocatalyst. After the addition of the *x*Ag@TPPQP CMP nanocatalyst, the signal at a wavelength of 400 nm decreased gradually, accompanied by the appearance of a new peak at 310 nm, representing the produced *p*-AP [Fig. 4(b)–(d)]. In addition, the reduction of *p*-nitrophenolate could be followed through the vanishing of the deep-yellow solution to colorless during the reduction process [Fig. 4e]. Because of the excess

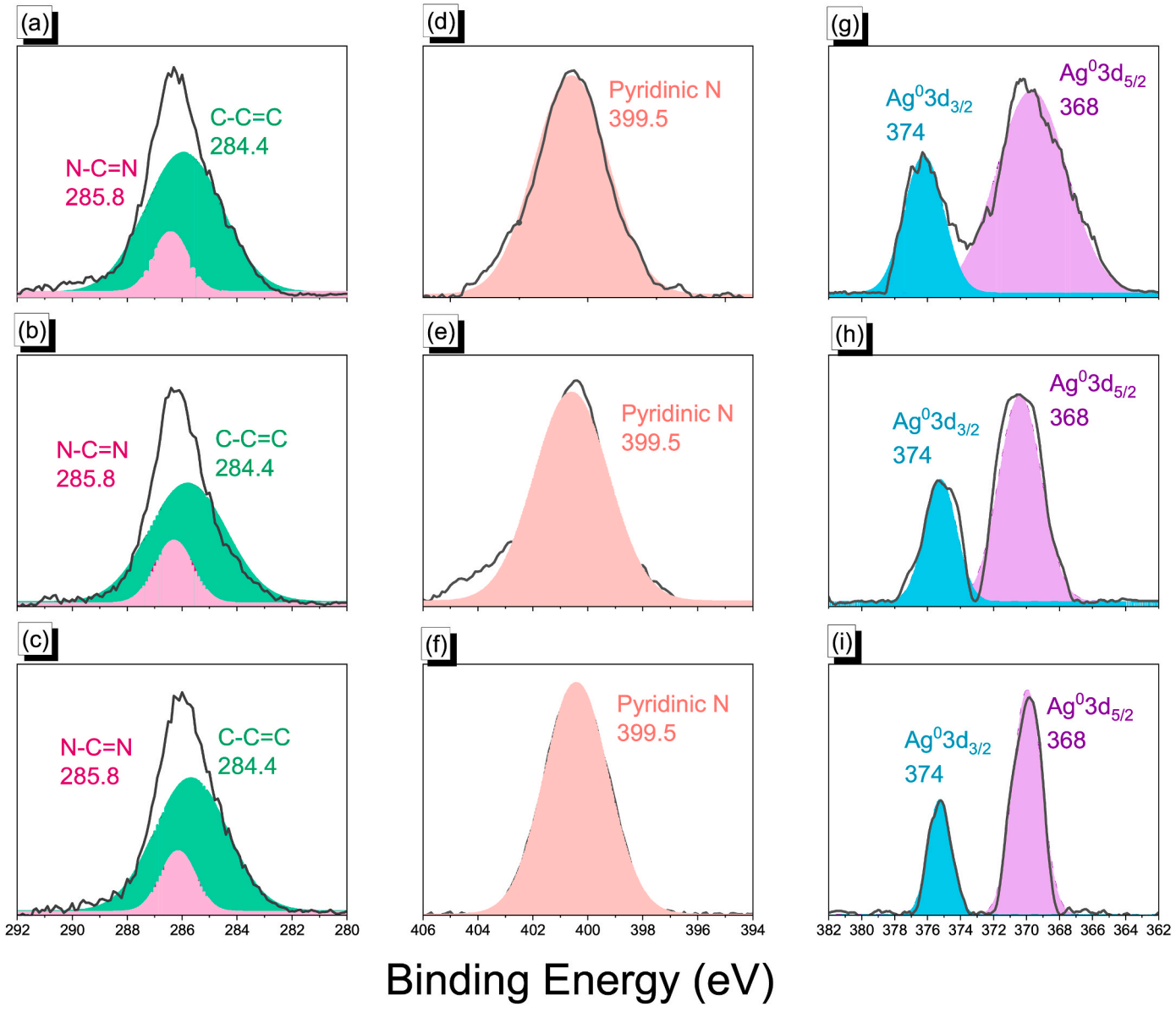

Fig. 3. High-resolution XPS spectra revealing the (a–c) C 1s, (d–f) N 1s, and (g–i) Ag 3d peaks for the (1, 3, and 5 wt%) Ag@TPPQP CMPs nanocatalysts.

concentration of $NaBH_4$, the reduction of *p*-NP to *p*-AP could be considered a reaction with pseudo-first-order kinetics, based on the equation

$$\ln(C/C_o) = k_{app} \times t \quad \text{(equation 1)}$$

Therefore, after plotting $\ln(C/C_o)$ with respect to time, the slope revealed the kinetic rate of reduction. The rates of reduction when using 0.5 mg of the 1Ag@TPPQP and 3Ag@TPPQP CMP nanocatalysts were 0.0097 and 0.0181 s^{-1}, respectively [Fig. 4(f) and (g)]. The normalized rate constants (k_{nor}) of the 1Ag@TPPQP and 3Ag@TPPQP CMP nanocatalysts were 19.4 and 36.2 mg^{-1} s^{-1}, respectively. We could not calculate the rate of reduction of *p*-NP mediated by the 5Ag@TPPQP CMP nanocatalyst because the color of *p*-NP vanished too quickly [Fig. 4 (d) and (h)]. The higher rates of reduction when using the 3Ag@TPPQP and 5Ag@TPPQP CMP nanocatalysts [Fig. 4(c) and (d)] were due to their higher loading percentages of Ag onto the TPPQP CMP [36,73]. Table S3 compares the efficacy of the 1Ag@TPPQP and 3Ag@TPPQP CMP nanocatalysts for the reduction of *p*-NP in the presence of $NaBH_4$ at standard temperature and pressure (STP) with those of other reported Ag-supported catalysts, including CMP [36], mesoporous silica (KIT) [74], and polyaniline [75]; gratifyingly, our Ag@TPPQP CMP nanocatalysts displayed the highest kinetic rates.

We suspected that the high kinetic rates of reduction of *p*-NP resulted from interactions between the phenolic OH group of *p*-NP and the pyridyl groups of the Ag@TPPQP CMP nanocatalysts [76]. Accordingly, we examined the reduction of *p*-FNB at the same ratios used for reduction of *p*-NP; we recorded a lower kinetic rate of 3×10^{-3} s^{-1} (Figs. S9–S10). The lower reduction performance toward *p*-FNB is consistent with the lower strength of the interactions between pyridyl groups and fluorine atoms [77]. This finding suggests a role for the pyridyl groups located on the TPPQP CMPs in the reduction of *p*-NP. Moreover, the 1Ag@TPPQP CMP nanocatalyst displayed high efficiency in the reduction of *p*-nitroaniline (*p*-NA) to *p*-aminoaniline (*p*-AA), as revealed in Fig. S11, with a high kinetic rate of 0.007 s^{-1} as clarified in Fig. S12.

3.5. Recovery of Ag@TPPQP CMPs

The potential industrial use of the 1Ag@TPPQP CMP catalyst would be boosted by its high recovery. Accordingly, we tested the recovery of the 1Ag@TPPQP CMP nanocatalyst through five consecutive cycles of

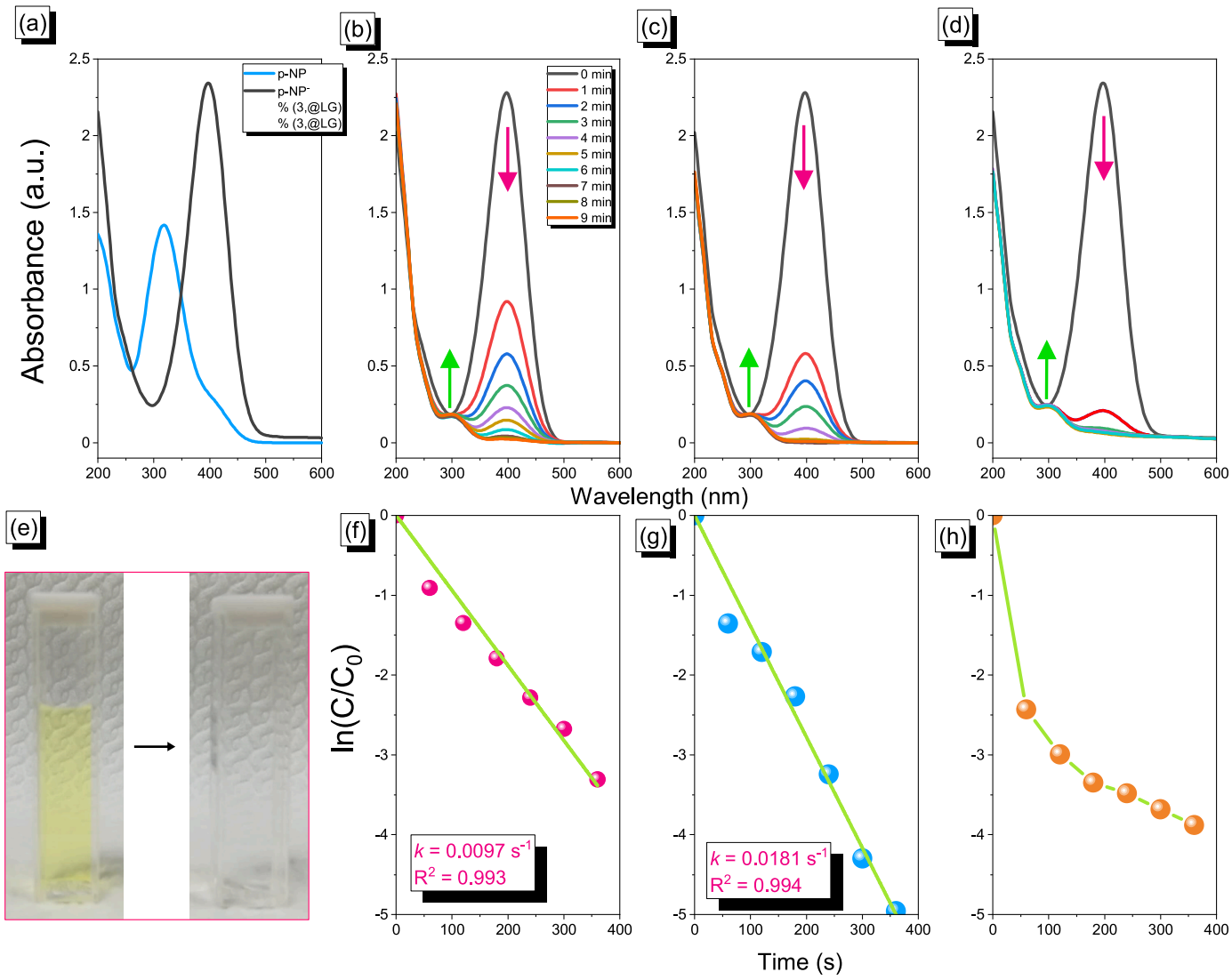

Fig. 4. UV–Vis spectra revealing (a) the conversion of *p*-NP to *p*-nitrophenolate and (b–d) the reduction of *p*-NP to *p*-AP when using the 1Ag@TPPQP, 3Ag@TPPQP, and 5Ag@TPPQP CMPs, respectively. (e) Fading yellow color during the transformation of *p*-NP to *p*-AP. (f–h) Pseudo-first-order kinetics of the reduction of *p*-NP over the (f) 1Ag@TPPQP, (g) 3Ag@TPPQP, and (h) 5Ag@TPPQP CMPs. (For interpretation of the references to color in this figure legend, the reader is referred to the Web version of this article.)

the reduction of *p*-NP (Fig. 5a). The 1Ag@TPPQP CMP nanocatalyst provided an efficacy rate of 90% even after the fifth cycle, suggesting a minor decrease in catalytic activity through only a meager loss of the nanocatalyst during the recovery processes. The high reusability implied high chemical stability for the Ag@TPPQP CMP nanocatalyst. Furthermore, the FITR spectra of the Ag@TPPQP CMP nanocatalyst recorded before and after recycling were identical (Fig. 5b). In addition, the TEM image of the 1Ag@TPPQP CMP nanocatalyst confirmed the stability of

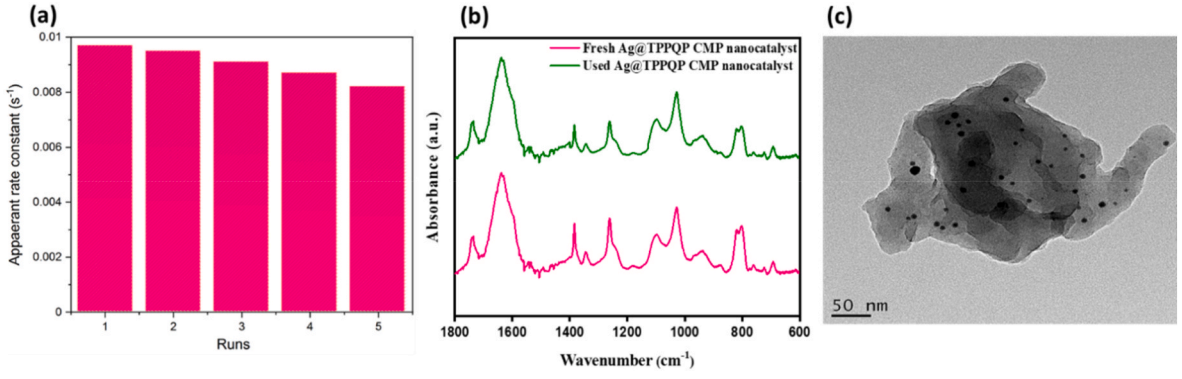

Fig. 5. (a) Recycling of the 1Ag@TPPQP CMP nanocatalyst over five periods of reduction. (b) FTIR spectrum and (c) TEM image of the Ag@TPPQP CMP nanocatalyst after reuse.

the Ag NPs at the surface of the TPPQP CMP. All of these features suggest that Ag@TPPQP CMPs are promising nanocatalysts for the reduction of nitrophenols, and addition to identifying the TPPQP CMP as an excellent substrate for decoration with noble metals.

4. Conclusions

We have prepared a pyridyl-based CMP (TPPQP CMP) through traditional Suzuki coupling and characterized it using FTIR spectroscopy, NMR spectroscopy, the BET method, TGA, SEM, and TEM. The pyridyl units of the TPPQP CMP facilitated the capture of Ag^{+} ions and their subsequent reduction into Ag NPs, thereby yielding Ag@TPPQP CMP nanocatalysts. The Ag@TPPQP CMPs appear to be highly suitable for disposing of priority pollutants, due to their excellent catalytic activity toward the reduction of nitroaromatic compounds at STP. They provided high values of k_{nor} (up to 36.2 mg^{-1} s^{-1}), due to the presence of many pyridyl groups that could interact with phenolic OH groups. Furthermore, the Ag@TPPQP CMPs displayed high recoveries without considerable losses of efficacy.

CRediT authorship contribution statement

Mohammed G. Kotp: Writing – original draft, Data curation, Formal analysis, Methodology. **Ahmed F.M. EL-Mahdy:** Writing – original draft, Supervision, Investigation, Data curation, Conceptualization. **Tzu-Ling Yang:** Data curation, Formal analysis. **Shiao-Wei Kuo:** Writing – review & editing, Supervision, Funding acquisition, Conceptualization.

Declaration of competing interest

There are no conflicts to declare.

Acknowledgements

This study was supported financially by Ministry of Science and Technology, Taiwan, under contracts MOST 108-2218-E-110-013-MY3 and 108-2221-E-110-014-MY3.

Appendix A. Supplementary data

Supplementary data to this article can be found online at https://doi.org/10.1016/j.micromeso.2021.111669.

References

[1] R. Guo, H. Liu, K. Yang, S. Wang, P. Sun, H. Gao, B. Wang, F. Chen, β-Cyclodextrin polymerized in cross-flowing channels of biomass sawdust for rapid and highly efficient pharmaceutical pollutants removal from water, ACS Appl. Mater. Interfaces 12 (2020) 32817–32826.
[2] E.P. Ferreira-Neto, S. Ullah, T.C. da Silva, R.R. Domeneguetti, A.P. Perissinotto, F. S. de Vicente, U.P. Rodrigues-Filho, S.J. Ribeiro, Bacterial nanocellulose/MoS2 hybrid aerogels as bifunctional adsorbent/photocatalyst membranes for in-flow water decontamination, ACS Appl. Mater. Interfaces 12 (2020) 41627–41643.
[3] Q. Sun, B. Aguila, Y. Song, S. Ma, Tailored porous organic polymers for task-specific water purification, Acc. Chem. Res. 53 (2020) 812–821.
[4] S. Mollick, S. Fajal, S. Saurabh, D. Mahato, S.K. Ghosh, Nanotrap grafted anion exchangeable hybrid materials for efficient removal of toxic oxoanions from water, ACS Cent. Sci. 6 (2020) 1534–1541.
[5] M. Zhang, X. Su, L. Ma, A. Khan, L. Wang, J. Wang, A. Maloletnev, C. Yang, Promotion effects of halloysite nanotubes on catalytic activity of Co3O4 nanoparticles toward reduction of 4-nitrophenol and organic dyes, J. Hazard Mater. 403 (2021) 123870.
[6] S. Jiang, L. Wang, Y. Duan, J. An, Q. Luo, Y. Zhang, Y. Tang, J. Huang, B. Zhang, J. Liu, A novel strategy to construct supported silver nanocomposite as an ultra-high efficient catalyst, Appl. Catal., B 283 (2021) 119592.
[7] V. Gemini, A. Gallego, V. De Oliveira, C. Gomez, G. Manfio, S. Korol, Biodegradation and detoxification of p-nitrophenol by Rhodococcus wratislaviensis, Int. Biodeterior. Biodegrad. 55 (2005) 103–108.
[8] B. Zhao, G. Mele, I. Pio, J. Li, L. Palmisano, G. Vasapollo, Degradation of 4-nitrophenol (4-NP) using Fe–TiO2 as a heterogeneous photo-Fenton catalyst, J. Hazard Mater. 176 (2010) 569–574.
[9] T.-L. Lai, K.-F. Yong, J.-W. Yu, J.-H. Chen, Y.-Y. Shu, C.-B. Wang, High efficiency degradation of 4-nitrophenol by microwave-enhanced catalytic method, J. Hazard Mater. 185 (2011) 366–372.
[10] J. Li, D. Kuang, Y. Feng, F. Zhang, Z. Xu, M. Liu, A graphene oxide-based electrochemical sensor for sensitive determination of 4-nitrophenol, J. Hazard Mater. 201 (2012) 250–259.
[11] M.M. Ayad, W.A. Amer, M.G. Kotp, Magnetic polyaniline-chitosan nanocomposite decorated with palladium nanoparticles for enhanced catalytic reduction of 4-nitrophenol, Mol. Catal. 439 (2017) 72–80.
[12] J. Luo, Y. Xu, J. Wang, L. Zhang, X. Jiang, J. Shen, Coupled biodegradation of p-nitrophenol and p-aminophenol in bioelectrochemical system: mechanism and microbial functional diversity, J. Environ. Sci. 108 (2021) 134–144.
[13] L. Bo, Y. Zhang, X. Quan, B. Zhao, Microwave assisted catalytic oxidation of p-nitrophenol in aqueous solution using carbon-supported copper catalyst, J. Hazard Mater. 153 (2008) 1201–1206.
[14] X. Wu, X. Song, H. Chen, J. Yu, Experimental study and quantum chemical calculation of free radical reactions in p-nitrophenol degradation during electrochemical oxidation process, J. Water Proc. Eng. 40 (2021) 101769.
[15] S. Yu, J. Hu, J. Wang, Gamma radiation-induced degradation of p-nitrophenol (PNP) in the presence of hydrogen peroxide (H2O2) in aqueous solution, J. Hazard Mater. 177 (2010) 1061–1067.
[16] Z. Ma, L. Zhu, X. Lu, S. Xing, Y. Wu, Y. Gao, Catalytic ozonation of p-nitrophenol over mesoporous Mn–Co–Fe oxide, Separ. Purif. Technol. 133 (2014) 357–364.
[17] D. Méndez, R. Vargas, C. Borrás, S. Blanco, J. Mostany, B.R. Scharifker, A rotating disk study of the photocatalytic oxidation of p-nitrophenol on phosphorus-modified TiO2 photocatalyst, Appl. Catal., B 166 (2015) 529–534.
[18] Z. Xiong, H. Zhang, W. Zhang, B. Lai, G. Yao, Removal of nitrophenols and their derivatives by chemical redox: a review, Chem. Eng. J. 359 (2019) 13–31.
[19] P. Fan, X. Zhang, H. Deng, X. Guan, Enhanced reduction of p-nitrophenol by zerovalent iron modified with carbon quantum dots, Appl. Catal., B 285 (2021) 119829.
[20] H. Wang, F. Lu, C. Ma, Y. Ma, M. Zhang, B. Wang, Y. Zhang, Y. Liu, H. Huang, Z. Kang, Carbon dots with positive surface charge from tartaric acid and m-aminophenol for selective killing of Gram-positive bacteria, J. Mater. Chem. B. 9 (2021) 125–130.
[21] K. Lewis, R. Wagner, S.E. Rodriguez-Cruz, M.J. Weaver, J.C. Dumke, Validation of the 4-aminophenol color test for the differentiation of marijuana-type and hemp-type cannabis, J. Forensic Sci. 66 (2021) 285–294.
[22] J. Otutu, D. Okoro, E. Ossai, Preparation of dis-azo dyes derived from p-aminophenol and their fastness properties for synthetic polymer-fibres, J. Appl. Sci. 8 (2008) 334–339.
[23] K. Takenaka, K. Kaneko, N. Takahashi, S. Nishimura, H. Kakeya, Retro-aza-Michael reaction of an o-aminophenol adduct in protic solvents inspired by natural products, Biorg, Med. Chem. 35 (2021) 116059.
[24] C. Rode, M. Vaidya, R. Chaudhari, Synthesis of p-aminophenol by catalytic hydrogenation of nitrobenzene, Org. Process Res. Dev. 3 (1999) 465–470.
[25] E. Hür, G. Bereket, B. Duran, D. Özdemir, Y. Şahin, Electropolymerization of m-aminophenol on mild steel and its corrosion protection effect, Prog. Org. Coating 60 (2007) 153–160.
[26] W.C. Chen, Y.T. Liu, S.W. Kuo, Mesoporous organic/inorganic hybrid materials with Frank-Kasper phases templated by an unusual linear symmetry diblock copolymer, Macromol. Rapid Commun. 42 (2021) 2100302.
[27] W.-C. Chen, Y.-T. Liu, S.-W. Kuo, Highly thermal stable phenolic resin based on double-decker-shaped POSS nanocomposites for supercapacitors, Polymers 12 (2020) 2151.
[28] W.-C. Chen, M.M. Ahmed, C.-F. Wang, C.-F. Huang, S.-W. Kuo, Highly thermally stable mesoporous Poly (cyanate ester) featuring double-decker–shaped polyhedral silsesquioxane framework, Polymer 185 (2019) 121940.
[29] W.-C. Chen, S.-W. Kuo, Ortho-imide and allyl groups effect on highly thermally stable polybenzoxazine/double-decker-shaped polyhedral silsesquioxane hybrids, Macromolecules 51 (2018) 9602–9612.
[30] M. Atarod, M. Nasrollahzadeh, S.M. Sajadi, Euphorbia heterophylla leaf extract mediated green synthesis of Ag/TiO2 nanocomposite and investigation of its excellent catalytic activity for reduction of variety of dyes in water, J. Colloid Interface Sci. 462 (2016) 272–279.
[31] Y. Duan, Y. Ma, Y. Xie, D. Li, D. Deng, C. Zhang, Y. Yang, Preparation of PdAuCu/C as a highly active catalyst for the reduction of 4-nitrophenol by controlling the deposition of noble metals, Chem. Asian J. 16 (2021) 165–173.
[32] Y. Wang, P. Gao, Y. Wei, Y. Jin, S. Sun, Z. Wang, Y. Jiang, Silver nanoparticles decorated magnetic polymer composites (Fe3O4@ PS@ Ag) as highly efficient reusable catalyst for the degradation of 4-nitrophenol and organic dyes, J. Environ. Manag. 278 (2021) 111473.
[33] A.N. Chishti, L. Ni, F. Guo, X. Lin, Y. Liu, H. Wu, M. Chen, G.W. Diao, Magnetite-Silica core-shell nanocomposites decorated with silver nanoparticles for enhanced catalytic reduction of 4-nitrophenol and degradation of methylene blue dye in the water, J. Environ. Chem. Eng. 9 (2021) 104948.
[34] H.D. Beyene, A.A. Werkneh, H.K. Bezabh, T.G. Ambaye, Synthesis paradigm and applications of silver nanoparticles (AgNPs), a review, Sustain Mater. Technol. 13 (2017) 18–23.
[35] D. Besold, S. Risse, Y. Lu, J. Dzubiella, M. Ballauff, Kinetics of the reduction of 4-nitrophenol by silver nanoparticles immobilized in thermoresponsive core–shell nanoreactors, Ind. Eng. Chem. Res. 60 (2021) 3922–3935.
[36] H.-L. Cao, H.-B. Huang, Z. Chen, B. Karadeniz, J. Lü, R. Cao, Ultrafine silver nanoparticles supported on a conjugated microporous polymer as high-performance nanocatalysts for nitrophenol reduction, ACS Appl. Mater. Interfaces 9 (2017) 5231–5236.

[37] R.-L. Wang, D.-P. Li, L.-J. Wang, X. Zhang, Z.-Y. Zhou, J.-L. Mu, Z.-M. Su, The preparation of new covalent organic framework embedded with silver nanoparticles and its applications in degradation of organic pollutants from waste water, Dalton Trans. 48 (2019) 1051–1059.
[38] A.M. Elewa, A.F.M. EL-Mahdy, M.H. Elsayed, M.G. Mohamed, S.-W. Kuo, H.-H. Chou, Sulfur-doped triazine-conjugated microporous polymers for achieving the robust visible-light-driven hydrogen evolution, Chem. Eng. J. 421 (2021) 129825.
[39] A.F.M. El-Mahdy, C.-H. Kuo, A. Alshehri, C. Young, Y. Yamauchi, J. Kim, S.-W. Kuo, Strategic design of triphenylamine-and triphenyltriazine-based two-dimensional covalent organic frameworks for CO 2 uptake and energy storage, J. Mater. Chem. 6 (2018) 19532–19541.
[40] S. Han, Z. Li, S. Ma, Y. Zhi, H. Xia, X. Chen, X. Liu, Bandgap engineering in benzotrithiophene-based conjugated microporous polymers: a strategy for screening metal-free heterogeneous photocatalysts, J. Mater. Chem. 9 (2021) 3333–3340.
[41] N. Baig, S. Shetty, S. Al-Mousawi, B. Alameddine, Conjugated microporous polymers using a copper-catalyzed [4+ 2] cyclobenzannulation reaction: promising materials for iodine and dye adsorption, Polym. Chem. 12 (2021) 2282–2292.
[42] L. Zhong, Z. Fang, C. Shu, C. Mo, X. Chen, D. Yu, Redox donor–acceptor conjugated microporous polymers as ultralong-lived organic anodes for rechargeable air batteries, Angew. Chem. Int. Ed. 60 (2021) 10164–10171.
[43] H.R. Abuzeid, A.F.M. EL-Mahdy, S.-W. Kuo, Covalent organic frameworks: design principles, synthetic strategies, and diverse applications, Giant 6 (2021) 100054.
[44] M.G. Mohamed, M.M. Ahmed, W.-T. Du, S.-W. Kuo, Meso/microporous carbons from conjugated hyper-crosslinked polymers based on tetraphenylethene for high-performance CO2 capture and supercapacitor, Molecules 26 (2021) 738.
[45] M.G. Mohamed, N.-Y. Liu, A.F.M. EL-Mahdy, S.-W. Kuo, Ultrastable luminescent hybrid microporous polymers based on polyhedral oligomeric silsesquioxane for CO2 uptake and metal ion sensing, Microporous Mesoporous Mater. 311 (2021) 110695.
[46] A.F.M. EL-Mahdy, A.M. Elewa, S.W. Huang, H.H. Chou, S.W. Kuo, Dual-function fluorescent covalent organic frameworks: HCl sensing and photocatalytic H2 evolution from water, Adv. Opt. Mater. 8 (2020) 2000641.
[47] M.G. Mohamed, C.-C. Lee, A.F.M. EL-Mahdy, J. Lüder, M.-H. Yu, Z. Li, Z. Zhu, C.-C. Chueh, S.-W. Kuo, Exploitation of two-dimensional conjugated covalent organic frameworks based on tetraphenylethylene with bicarbazole and pyrene units and applications in perovskite solar cells, J. Mater. Chem. 8 (2020) 11448–11459.
[48] A.F.M. El-Mahdy, C. Young, J. Kim, J. You, Y. Yamauchi, S.-W. Kuo, Hollow microspherical and microtubular [3+ 3] carbazole-based covalent organic frameworks and their gas and energy storage applications, ACS Appl. Mater. Interfaces 11 (2019) 9343–9354.
[49] M.G. Mohamed, E.C. Atayde Jr., B.M. Matsagar, J. Na, Y. Yamauchi, K.C.-W. Wu, S.-W. Kuo, Construction hierarchically mesoporous/microporous materials based on block copolymer and covalent organic framework, J. Taiwan Inst. Chem. Eng. 112 (2020) 180–192.
[50] M.G. Mohamed, M.H. Elsayed, A.M. Elewa, A.F.M. EL-Mahdy, C.-H. Yang, A. A. Mohammed, H.-H. Chou, S.-W. Kuo, Pyrene-containing conjugated organic microporous polymers for photocatalytic hydrogen evolution from water, Catal. Sci. Technol. 11 (2021) 2229–2241.
[51] A.A. Guilbert, Y. Bai, C.M. Aitchison, R.S. Sprick, M. Zbiri, Impact of chemical structure on the dynamics of mass transfer of water in conjugated microporous polymers: a neutron spectroscopy study, ACS Appl. Polym. Mater. 3 (2021) 765–776.
[52] M.M. Bai, H.V. Babu, V. Lakshmi, M.R. Rao, Structure–property–function relationship of fluorescent conjugated microporous polymers, Mater. Chem. Front. 5 (2021) 2506–2551.
[53] M.G. Mohamed, T.-C. Chen, S.-W. Kuo, Solid-state chemical transformations to enhance gas capture in benzoxazine-linked conjugated microporous polymers, Macromolecules 12 (2021) 5866–5877.
[54] H. Xu, X. Li, H. Hao, X. Dong, W. Sheng, X. Lang, Designing fluorene-based conjugated microporous polymers for blue light-driven photocatalytic selective oxidation of amines with oxygen, Appl. Catal., B 285 (2021) 119796.
[55] X. Lan, X. Liu, Y. Zhang, Q. Li, J. Wang, Q. Zhang, G. Bai, Unveiling charge dynamics in acetylene-bridged Donor− π–acceptor covalent triazine framework for enhanced photoredox catalysis, ACS Catal. 11 (2021) 7429–7441.
[56] M.M. Samy, M.G. Mohamed, A.F.M. El-Mahdy, T.H. Mansoure, K.C.-W. Wu, S.-W. Kuo, High-performance supercapacitor electrodes prepared from dispersions of tetrabenzonaphthalene-based conjugated microporous polymers and carbon nanotubes, ACS Appl. Mater. Interfaces 13 (2021) 51906–51916.
[57] M.G. Mohamed, A.F.M. EL-Mahdy, Y. Takashi, S.-W. Kuo, Ultrastable conductive microporous covalent triazine frameworks based on pyrene moieties provide high-performance CO 2 uptake and supercapacitance, New J. Chem. 44 (2020) 8241–8253.
[58] A.F.M EL-Mahdy, J. Lüder, M.G. Kotp, S.-W. Kuo, A Tröger's base-derived covalent organic polymer containing carbazole units as a high-performance supercapacitor, Polymers 13 (2021) 1385.
[59] A. Singh, P. Verma, S. Laha, D. Samanta, S. Roy, T.K. Maji, Photochromic conjugated microporous polymer manifesting bio-inspired pcFRET and logic gate functioning, ACS Appl. Mater. Interfaces 12 (2020) 20991–20997.
[60] M.G. Kotp, A.M. Elewa, A.F. EL-Mahdy, H.-H. Chou, S.-W. Kuo, Tunable pyridyl-based conjugated microporous polymers for visible light-driven hydrogen evolution, ACS Appl. Energy Mater. 4 (2021) 13140–13151.
[61] T.-L. Lee, A.M. Elewa, M.G. Kotp, H.-H. Chou, A.F.M. EL-Mahdy, Carbazole-and thiophene-containing conjugated microporous polymers with different planarity for enhanced photocatalytic hydrogen evolution, Chem. Commun. 57 (2021) 11968–11971.
[62] Y.B. Zhou, Z.P. Zhan, Conjugated microporous polymers for heterogeneous catalysis, Chem. Asian J. 13 (2018) 9–19.
[63] X. Zhang, B. Qiu, Y. Zou, S. Wang, W. Mai, Y. Cao, Y. Wang, J. Chen, T. Li, Green synthesized cobalt-bipyridine constructed conjugated microporous polymer: an efficient heterogeneous catalyst for cycloaddition of epoxides via CO2 fixation under ambient conditions, Microporous Mesoporous Mater. 319 (2021) 110758.
[64] W. Gong, Q. Wu, G. Jiang, G. Li, Ultrafine silver nanoparticles supported on a covalent carbazole framework as high-efficiency nanocatalysts for nitrophenol reduction, J. Mater. Chem. 7 (2019) 13449–13454.
[65] W. Liu, X. Luo, Y. Bao, Y.P. Liu, G.-H. Ning, I. Abdelwahab, L. Li, C.T. Nai, Z.G. Hu, D. Zhao, A two-dimensional conjugated aromatic polymer via C–C coupling reaction, Nat. Chem. 9 (2017) 563–570.
[66] W. Liu, M. Ulaganathan, I. Abdelwahab, X. Luo, Z. Chen, S.J. Rong Tan, X. Wang, Y. Liu, D. Geng, Y. Bao, Two-dimensional polymer synthesized via solid-state polymerization for high-performance supercapacitors, ACS Nano 12 (2018) 852–860.
[67] B. Baruah, G.J. Gabriel, M.J. Akbashev, M.E. Booher, Facile synthesis of silver nanoparticles stabilized by cationic polynorbornenes and their catalytic activity in 4-nitrophenol reduction, Langmuir 29 (2013) 4225–4234.
[68] R. Patil, M. Kokate, P. Salvi, S. Kolekar, A novel one step synthesis of silver nanoparticles using room temperature ionic liquid and their biocidal activity, CR CHIM 14 (2011) 1122–1127.
[69] R. Manno, V. Sebastian, S. Irusta, R. Mallada, J. Santamaria, Ultra-small silver nanoparticles immobilized in mesoporous SBA-15. Microwave-assisted synthesis and catalytic activity in the 4-nitrophenol reduction, Catal. Today 362 (2021) 81–89.
[70] M.M. Ayad, W.A. Amer, M.G. Kotp, I.M. Minisy, A.F. Rehab, D. Kopecký, P. Fitl, Synthesis of silver-anchored polyaniline–chitosan magnetic nanocomposite: a smart system for catalysis, RSC Adv. 7 (2017) 18553–18560.
[71] P. Zhao, X. Feng, D. Huang, G. Yang, D. Astruc, Basic concepts and recent advances in nitrophenol reduction by gold-and other transition metal nanoparticles, Coord. Chem. Rev. 287 (2015) 114–136.
[72] S. Wunder, F. Polzer, Y. Lu, Y. Mei, M. Ballauff, Kinetic analysis of catalytic reduction of 4-nitrophenol by metallic nanoparticles immobilized in spherical polyelectrolyte brushes, J. Phys. Chem. C 114 (2010) 8814–8820.
[73] A. Sangili, M. Annalakshmi, S.-M. Chen, P. Balasubramanian, M. Sundrarajan, Synthesis of silver nanoparticles decorated on core-shell structured tannic acid-coated iron oxide nanospheres for excellent electrochemical detection and efficient catalytic reduction of hazardous 4-nitrophenol, Compos. B Eng. 162 (2019) 33–42.
[74] M.M. Ayad, N.L. Torad, A.A. El-Nasr, W.A. Amer, Study on catalytic efficiency of platinum and silver nanoparticles confined in nanosized channels of a 3-D mesostructured silica, J. Porous Mater. 28 (2021) 65–79.
[75] K.M. Manesh, A.I. Gopalan, K.-P. Lee, S. Komathi, Silver nanoparticles distributed into polyaniline bridged silica network: a functional nanocatalyst having synergistic influence for catalysis, Catal. Commun. 11 (2010) 913–918.
[76] I. Ahmad, A.A. Ganie, A.A. Dar, Achievement of enhanced solubility and improved optics in molecular complexes based on a sulfonate–pyridinium supramolecular synthon, CrystEngComm 22 (2020) 3933–3942.
[77] A. Kumar, B. Mishra, B.P. Tripathi, Polydopamine assisted synthesis of ultrafine silver nanoparticles for heterogeneous catalysis and water remediation, Nano-Struct. Nano-Objects 23 (2020) 100489.